Magnetic Image Sensor for Detecting Ferrous Contaminants in Nonferrous Scraps

Wu, Yongli; Oudshoorn, Tijmen; Mulder, Rik; Van Beek, Kees; Rem, Peter

DOI
10.1109/JSEN.2024.3457799

Publication date
2024

Document Version
Final published version

Published in
IEEE Sensors Journal

Magnetic Image Sensor for Detecting Ferrous Contaminants in Nonferrous Scraps

Yongli Wu, Tijmen Oudshoorn, Rik Mulder, Kees van Beek, and Peter Rem

***Abstract*—The high-precision scrap sorting for effective metal recycling can bring substantial environmental and economic benefits. This article presents a magnetic image sensor that can help to identify the ferrous contaminants inside nonferrous scraps of large sizes. First, the concept and the theory for detecting ferrous contaminants are described. In particular, an inversion algorithm is proposed to characterize the size and position of ferrous contaminants inside the main scrap bodies. Then, based on computed and measured results, the feasibility of sensor design using either 1-D Hall arrays or 1-D pickup coils is demonstrated. Finally, methods are suggested to minimize disturbing signals from very large nonferrous pieces passing through the slightly uneven magnetic field. The obtained findings in this study may apply not only to nonferrous scraps but many other materials of which the mass ratio of the ferrous contaminant to the main material is small.**

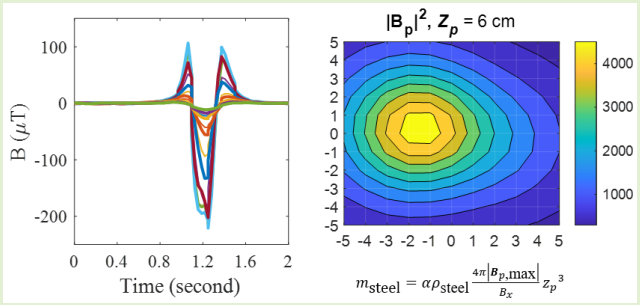

***Index Terms*— Ferrous contaminants, magnetic image sensor, metal recycling, metal scrap, scrap sorting.**

I. Introduction

NONFERROUS metals (e.g., aluminum, copper) are widely used in our daily life and industries, such as transportation, building, packaging, electricity transmission, and machinery [1]. Considering the enormous consumption of nonferrous metals worldwide, high-end recycling of nonferrous metals, with near-complete value recovery of the material into new products, is critical to the sustainability and circular economy of our world [1], [2], [3], [4]. To this end, scrap from end-of-life products must be sorted into different types by their properties, before going into the smelters to produce new alloys.

Shredding end-of-life (metal) products into scraps is an energy-intensive and expensive process. Thus, the larger the size of the shredded scrap is, the more environmental and economic benefits are obtained. On the other hand, scraps with large sizes (e.g., screen passing size 100–180 mm) may not be fully liberated from undesired attachments, such as screws and bolts. Instead, such attachments may stay as contaminants/inclusions in the scrap bodies. A very common type of attachment is a bolt or ring, nut, screw, and so on made from ferrous materials (e.g., iron and steel). Ferrous contaminants in nonferrous scraps can potentially damage the equipment in the eddy current separation process and can also seriously deteriorate the quality of the subsequently produced alloys [5]. Hence, such ferrous contaminants must be effectively identified and eliminated in the scrap sorting process for re-shredding. Standard magnetic separation processes [6], [7] are able to take ferrous scraps or nonferrous scraps with a large ferrous-to-nonferrous mass ratio from the scrap flow but not able to consistently separate scraps with a small ferrous-to-nonferrous mass ratio.

To identify small ferrous contaminants, sorting processes may rely on advanced technologies such as sensors and artificial intelligence (AI). With the fast development of computation technologies, AI or computer vision has become promising in the real-time recognition of scrap types [8], [9]. However, AI recognition relies on the analysis of the visual images of scraps; it can possibly identify contaminants visible to the cameras but cannot detect those underneath the surface of a scrap. Among sensor technologies, laser-induced breakdown spectroscopy (LIBS) [10], [11] is a powerful technique that can analyze the chemical elements of scraps. Nevertheless, LIBS may just give very few shots on a scrap in a real-time inspection of a processing line, and thus, the probability of successfully identifying small ferrous contaminants in a scrap

Received 12 August 2024; revised 22 August 2024; accepted 22 August 2024. Date of publication 12 September 2024; date of current version 31 October 2024. This work was supported in part by Dutch Company Myne Circular Metals (Formerly Reukema) and in part by EU Horizon Marie Skłodowska-Curie Project (SortCAS) under Grant 101066062. The associate editor coordinating the review of this article and approving it for publication was Prof. Kai Wu. *(Corresponding author: Yongli Wu.)*

Yongli Wu, Kees van Beek, and Peter Rem are with the Faculty of Civil Engineering and Geosciences, Delft University of Technology, 2628 CN Delft, The Netherlands (e-mail: y.wu-7@tudelft.nl).

Tijmen Oudshoorn and Rik Mulder are with Myne Circular Metals, 3846 BP Harderwijk, The Netherlands.

Digital Object Identifier 10.1109/JSEN.2024.3457799

body is very low. By comparison, X-ray transmission (XRT) can identify the contaminants inside scraps based on the differences in atomic density of materials [12]. However, for such sensor systems (e.g., LIBS and XRT), they are expensive in the equipment and operations and also require specific algorithms to interpret the data into meaningful information. Moreover, when the issue comes to the estimation of the mass/weight of the contaminants (which is important for estimating the purity of the sorted scraps), it becomes more difficult for AI and sensors.

Among various sensors, previous studies have shown that sensors based on electromagnetic induction [13] or magnetic induction [14] are effective in classifying nonferrous metal scraps, due to their differentiated properties (e.g., electric conductivity). Considering the unique ferromagnetic properties of ferrous objects, sensors based on proper magnetic techniques are also promising for identifying those ferrous contaminants. In particular, considering a ferromagnetic object as a magnetic dipole, its generated magnetic field is a function related to its magnetic moment and the relative distance to it [15], [16]; based on that, many magnetic detection techniques (e.g., magnetic anomaly detection (MAD) [17], [18]) have been developed and widely used in the past, e.g., in geological exploration [19] and detection or localization of ferromagnetic objects such as submarines [20] and vehicles [21]. In addition, various magnetic field sensors (e.g., Hall effect and anisotropic magnetoresistive sensors) have also been developed and used in diverse applications, such as consumer electronics, healthcare, and navigation [22], [23]. Some of the magnetic field sensors own the merits of high sensitivity, low power consumption, flexible substrates, and miniaturization [23] while maintaining a low cost. Nevertheless, the use of magnetic sensors in detecting ferrous contaminants in the nonferrous scrap recycling process should be both efficient and cost-effective, compared with AI and/or some advanced sensors (e.g., LIBS and XRT), but it has not been reported yet.

In this article, we will present a magnetic image sensor, which can recognize the size and position of ferrous contaminants in nonferrous scraps, thus helping to realize high-precision scrap sorting applications [24], [25], [26], [27], [28]. Since aluminum is the typical and most widely used nonferrous metal, it is taken as an example of nonferrous materials to test and demonstrate this sensor. Hence, in the following, the experiments and data are based on aluminum scraps with certain ferrous contaminants.

Next, the design and theory for the detection of ferrous contaminants in the presence of nonferrous materials (with aluminum as an example) will be introduced in Section II. Section III will describe the data interpretation and signal processing, illustrated and discussed with some experimental results. Finally, a full summary of the results and possible extensions will be given in Section IV.

II. Design and Theory for the Detection of Ferrous Contaminants

A. Design of the Magnetic Image Sensor

The schematic of the magnetic image sensor and its layout is shown in Fig. 1. It consists of two main parts:

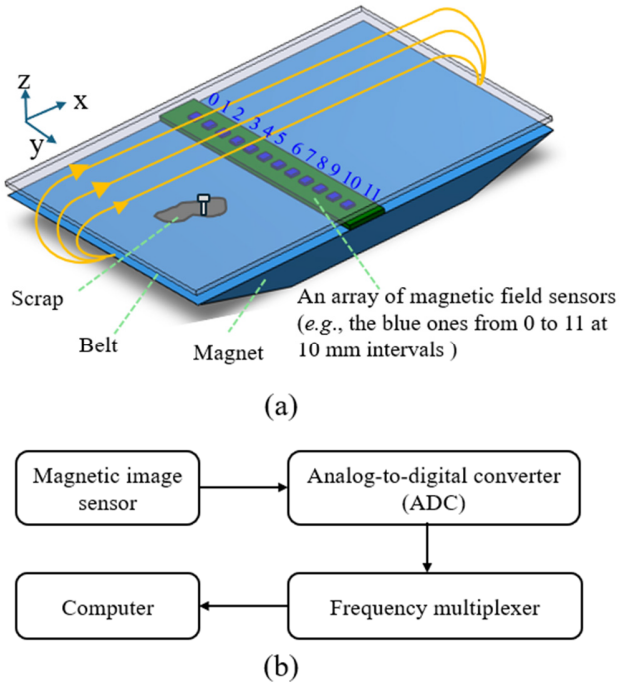

Fig. 1. Design of the magnetic image sensor. (a) Schematic of the components and layout. (b) Signal collection and transfer from the sensor to the computer.

1) A magnet below the conveyor belt, producing an almost homogeneous magnetic field in the sensor region, with field lines (yellow arrows) running parallel (or antiparallel) to the direction of motion of the conveyor belt;
2) An array of magnetic field sensors across the width of the detection region, directly below the belt.

Ideally, a homogeneous magnetic field magnetizes pieces of ferrous parts, while it does not attract them. Also, a piece of nonferrous metal will not produce eddy currents while moving in a homogeneous field. Therefore, ferrous parts produce a magnetic field and nonferrous parts do not. Unfortunately, it is not practically possible to extend a homogeneous magnetic field over a very long stretch of the belt. Therefore, ferrous parts will feel an attractive force and the nonferrous parts will produce eddy currents when entering the field or leaving the field zone. These effects are minimized by making the field transitions at entry and exit very smooth. As a result, the array of field sensors located in the middle of the homogeneous part of the field will detect the magnetized ferrous parts but not the nonferrous metal.

As shown schematically in Fig. 2, a ferrous part (gray cylinder) magnetizes in a magnetic field $\boldsymbol{B}$; within the homogeneous part of the field (yellow vectors), its magnetic moment $\boldsymbol{m}$ (green vector) has a constant value and direction. This magnetic moment creates a weak magnetic field $\boldsymbol{B}_p$ near the belt surface and the pattern of this field moves over the array of sensors (single sensor drawn in blue), for which the field patterns can be measured for the detection of ferrous pieces.

In the first experiment, a strip of 3-D Hall sensors [Fig. 1(a)] was selected for measuring the 3-D field pattern (B_{px}, B_{py}, and B_{pz}) of ferrous pieces p. Such Hall sensors are from Honeywell (type SS49E), with a sensitivity of about 1.4 mV/Gauss; they were selected because of their: 1) small

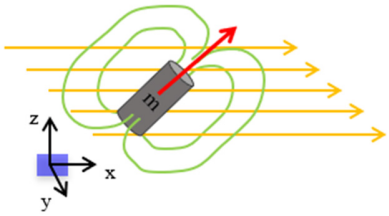

Fig. 2. Magnetic field (green lines) as a result of the magnetization of a ferrous cylinder (gray) in the homogeneous field of the magnet (yellow vectors).

size that can allow a compact implementation of a series of sensors (i.e., sensor array) in the setup; 2) linearity in response to the magnetic field; and 3) low cost when a series of sensors are used. Since ferrous parts and their fields are moving with respect to the sensors, it is also possible to detect the field by an array of pickup coils instead of Hall sensors. This was tried in the second experiment, using a wire-wound inductor that has a ferrite core; it has a rather high inductance (10 mH), which gives more sensitivity, and the ferrite core has open ends so that it is sensitive to external magnetic fields. In addition, other sensors, such as magnetoresistive or fluxgate sensors, may also be applicable to this application, and they may be studied in future work.

As shown in Fig. 1(b), the signal data from sensors are collected by an analog-to-digital converter (ADC), of which the type is NI 6255, with an ADC resolution of 16 bits. Then, the data from ADC are selected by a Texas Instruments multiplexer at a specified sampling rate before it is transformed into a computer for data processing. Note that different sampling rates can be set to achieve specific resolutions (pixel sizes) of the magnetic field patterns, considering the moving speed of the scrap or the belt.

B. Theory for Detecting the Ferrous Piece

In order to interpret the measured field data of a ferrous piece into its location $\boldsymbol{r}$ (i.e., the relative position to the sensor) and mass m_p, a mathematical problem needs to be solved, which is known as inversion [29]. As the field pattern of a ferrous piece is affected by multiple variables, including size/volume, shape, orientation, and position, the inverse problem of identifying the location and mass of a ferrous piece from the field pattern is complex, and different ferrous objects at different conditions may produce the same pattern. Therefore, simplifying assumptions about the nature of the ferrous piece(s) is needed to perform the inversion. Accordingly, we considered only cylindrically symmetric steel objects, which, however, represented the common ferrous contaminants (such as screws, rings, and nuts), as shown in the sample set in Fig. 3(a).

For the considered cylindrically symmetric shapes, their demagnetization factors along three principal axes are represented by D_a, D_b, and D_c. In this case, the "a"-direction is chosen as the axis of rotational symmetry, resulting in $D_b = D_c$ [Fig. 3(c)]. The major difference between cylinders and rings is the value of the dominant demagnetization factor.

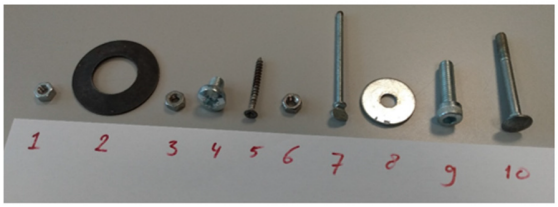

(a)

No.	Shape	Mass [g]
1	Nut	2.2
2	Ring	14.1
3	Nut	2.2
4	Bolt	10.7
5	Screw	2.2
6	Nut	2.2
7	Bolt	6.3
8	Ring	8.4
9	Bolt	15.9
10	Bolt	14.8

(b)

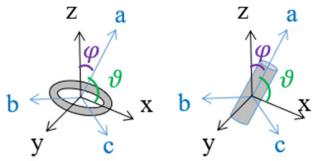

(c)

Fig. 3. Ferrous contaminants. (a) Sample set tested in experiments. (b) Shape and mass information of the sample set. (c) Principal axes of magnetization for two representative shapes.

1) *Screw and Bolt:* D_a is small (dominant), $D_b = D_c \approx 0.5$.
2) *Ring and Pop:* $D_b = D_c$ are small (dominant), $D_a \approx 1$.
3) *Nut:* $D_a \approx 0.5$ and D_b and $D_c \approx 0.25$.

The sum of the demagnetization factors always equals one, i.e., $D_a + D_b + D_c = 1$. For these types of ferrous objects, the mathematical forms of the shape tensor $\boldsymbol{N}$ and the orientation matrix $\boldsymbol{E}$ can be expressed as

$$\boldsymbol{N} = \begin{pmatrix} \frac{1}{D_a} & 0 & 0 \\ 0 & \frac{1}{D_b} & 0 \\ 0 & 0 & \frac{1}{D_c} \end{pmatrix} = \begin{pmatrix} \frac{1}{D_a} & 0 & 0 \\ 0 & \frac{1}{D_b} & 0 \\ 0 & 0 & \frac{1}{D_b} \end{pmatrix} \quad (1)$$

and

$$\boldsymbol{E} = \begin{pmatrix} \cos\vartheta & \sin\vartheta\sin\varphi & \sin\vartheta\cos\varphi \\ 0 & \cos\varphi & -\sin\varphi \\ -\sin\vartheta & \cos\vartheta\sin\varphi & \cos\vartheta\cos\varphi \end{pmatrix} \quad 0 \le \vartheta \le \frac{\pi}{2} \text{ and } 0 \le \varphi < 2\pi. \quad (2)$$

In these expressions, the angle ϑ is the angle between the rotational axis of symmetry (principal axis "a") of the piece and the x-axis. The angle φ is the angle between the x"a" plane and the xz plane.

If a ferrous object with volume V_p, the shape tensor $\boldsymbol{N}$, and the orientation matrix $\boldsymbol{E}$ is placed in a low-intensity magnetic field $\boldsymbol{B}$ [T], it will produce a magnetic moment $\boldsymbol{m}$ [Am^2], which is expressed as

$$\boldsymbol{m} = \frac{V_p}{\mu_0}\boldsymbol{E}^{-1} \cdot \boldsymbol{N} \cdot \boldsymbol{E} \cdot \boldsymbol{B}; \quad \mu_0 = 4\pi 10^{-7} \text{ (SI units)}. \quad (3)$$

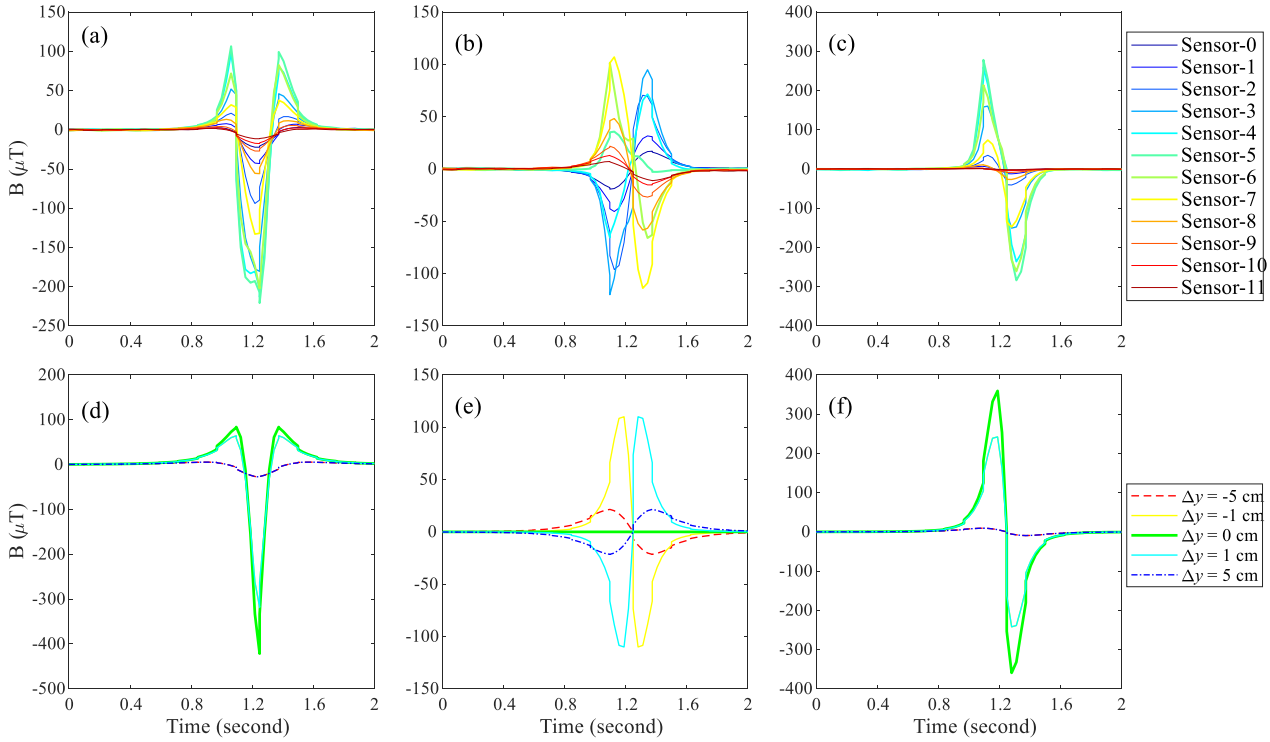

Fig. 4. $B_{p,x}$, $B_{p,y}$, and $B_{p,z}$ components (a)–(c) measured and (d)–(f) computed under the same condition: sampling rate at 40 Hz for a steel nut (No. 1 in the sample set) with a velocity $v = 0.2$ m/s over the sensor.

In the case of the current sensor design, the magnetic field is in the x-direction (i.e., $B_x \approx 0.050$ T and $B_y = B_z \approx 0$), so

$$\boldsymbol{m} = \frac{V_p B_x}{\mu_0} \begin{pmatrix} \frac{1}{D_b} + \cos^2\vartheta \left(\frac{1}{D_a} - \frac{1}{D_b}\right) \\ \sin\vartheta \cos\vartheta \sin\varphi \left(\frac{1}{D_a} - \frac{1}{D_b}\right) \\ \sin\vartheta \cos\vartheta \cos\varphi \left(\frac{1}{D_a} - \frac{1}{D_b}\right) \end{pmatrix}. \quad (4)$$

If the ferrous piece passes the sensor array with belt velocity v at time t_p, with a relative position $\boldsymbol{r}$ to the ith sensor of the array (at a height difference Δz above the sensor and at the distance difference $\Delta y_i = y_p - y_{\text{sensor},i}$ along the y-direction), the field $\boldsymbol{B}_p$ measured by this sensor can be given as [15]

$$\boldsymbol{B}_p = \left(B_{px}, B_{py}, B_{pz}\right) = \frac{\mu_0}{4\pi}\left(\frac{3(\boldsymbol{m}\cdot\boldsymbol{r})\boldsymbol{r}}{|\boldsymbol{r}|^5} - \frac{\boldsymbol{m}}{|\boldsymbol{r}|^3}\right)$$
$$\boldsymbol{r} = -\left(v\left(t - t_p\right), \Delta y_i, \Delta z\right). \quad (5)$$

As an example to show how the above theory can be applied to ferrous object detection, we consider a steel nut passing over the sensor line at a velocity, with its axis of rotation in the z-direction (so $\vartheta = (\pi/2), \varphi = 0$). Then, combining (4) and (5), the field can be expressed as (a detailed derivation is given in Appendix I)

$$\left(B_{px}, B_{py}, B_{pz}\right) = \frac{V_p B_x}{4\pi D_b\left(v^2\left(t - t_p\right)^2 + \Delta y_i^2 + \Delta z^2\right)^{2.5}} \times \begin{pmatrix} 2v^2\left(t - t_p\right)^2 - \Delta y_i^2 - \Delta z^2 \\ 3v\left(t - t_p\right)\Delta y_i \\ 3v\left(t - t_p\right)\Delta z \end{pmatrix}. \quad (6)$$

This example was considered in the first experiment with the sensor measurement of the steel nut [No. 1 in the sample set, Fig. 3(b)] of $V_p = 0.28$ cm^3 passing $\Delta z = 22$ mm over the sensor line with $v = 0.2$ m/s. The measured data are shown in Fig. 4, together with the computed data from the equation above for five sensors with different relative positions (Δy) to the path of the nut over the array. First, distinct peaks/valleys of the signals (e.g., about 50 μT higher or lower than that without ferrous objects) are shown in the results, indicating the detection of ferrous objects. Second, the computed results are generally close to the measured results. The comparison of the measured and the computed illustrates that the significance of signals varies for different sensors, due to the difference in their relative positions to the ferrous objects along the y-direction (Δy). In practice, to guarantee a good signal collection regardless of the y-coordinates of the ferrous objects, the sensor array needs to cover the full width of the belt that the scraps pass over. For the considered application, the design was to implement two 1-D Hall sensor arrays of 38 elements each, at 10-mm intervals across the width of the magnet, one array to the left of the guiding track of the belt and one array to the right (see Fig. 13).

III. Data Interpretation and Signal Processing

A. Field Pattern of a Ferrous Piece in a Homogeneous Field

In the actual practice of a sorting line, scraps will move at high velocity over the sensor. If the field of a ferrous object moving at a velocity of 2.5 m/s is sampled at a frequency of 250 Hz using a sensor array with sensors spaced at 1 cm,

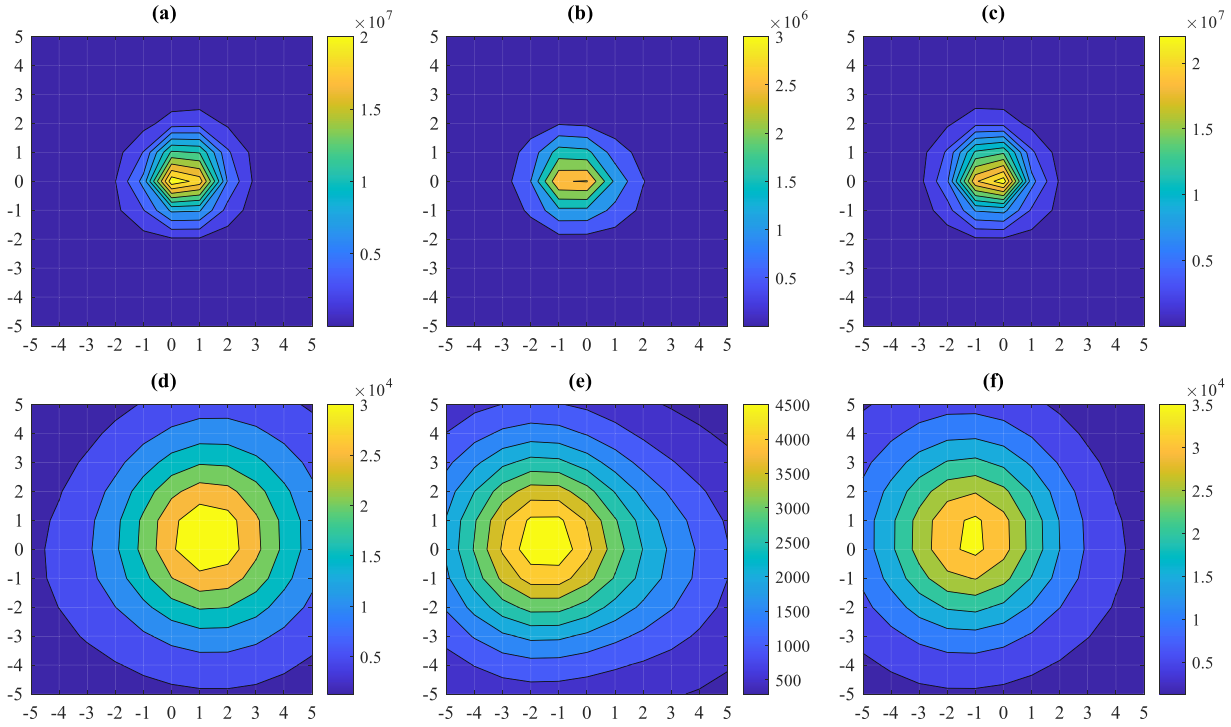

Fig. 5. Patterns of $|\boldsymbol{B}_p|^2$ in μT^2, for a bolt (left column), a nut (middle column), and a ring (right column) of 1 cm^3 of steel (about 8 g), located precisely above the center, at 2 cm (top row) and 6 cm (bottom row) height above the sensor plane. Pixels are square with a size of 1 cm^2. (a) Bolt, $Z_p = 2$ cm. (b) Nut, $Z_p = 2$ cm. (c) Ring $Z_p = 2$ cm. (d) Bolt, $Z_p = 6$ cm. (e) Nut, $Z_p = 6$ cm. (f) Ring $Z_p = 6$ cm.

this will produce a field pattern on a grid of 1×1 cm^2. It is also supposed that some region in the grid carries a signal of $|\boldsymbol{B}_p|^2$ that exceeds the noise threshold. Then, the issue is how to interpret the data in that region into an estimate of the mass and the position of the ferrous object. To reach the interpretation, the experimental tests are first conducted for collecting the signals of the ferrous objects with known size/mass (in the range of 2–16 g, as shown in the sample set in Fig. 3) and positions within 100 mm from the surface of the conveyor belt.

As a first step, we plot the computed contours of $|\boldsymbol{B}_p|^2$ in a 10×10 cm^2 area in the sensor plane, for a bolt, a nut, and a ring, each with a volume of 1 cm^3 of steel (7.8 g) and with their primary magnetic axes oriented so that $\vartheta = 45°$ and $\varphi = 30°$. Fig. 5 shows the results for two different heights, 20 and 60 mm, of the objects above the sensor plane. The equation for $|\boldsymbol{B}_p|^2$ is

$$\begin{aligned} \left|\boldsymbol{B}_p\right|^2 &= \frac{\mu_0^2 m^2}{16\pi^2 r^6}\left(1 + 3(\boldsymbol{e_m} \cdot \boldsymbol{e_r})^2\right) \\ \boldsymbol{e_m} &= \frac{\boldsymbol{m}}{|\boldsymbol{m}|}; \quad \boldsymbol{e_r} = \frac{\boldsymbol{r}}{|\boldsymbol{r}|}. \end{aligned} \tag{7}$$

The graphs show that $|\boldsymbol{B}_p|^2$ has almost circular contours and the centers of the circles (the maxima of $|\boldsymbol{B}_p|^2$) are typically within 1 cm from the projection of the position of the steel piece on the sensor plane, regardless of the piece's shape or orientation.

Starting from the maximum, the value of the $|\boldsymbol{B}_p|^2$ signal in (7) decays by a factor of about 8 at a radius equal to the height z_p of the piece above the sensor plane (Table I). This feature can be understood by the factor

$$\frac{\mu_0^2}{16\pi^2 r^6} = \frac{\mu_0^2}{16\pi^2\left(x^2 + y^2 + z_p^2\right)^3} \xrightarrow{x^2+y^2=z^2} \frac{1}{8}\frac{\mu_0^2}{16\pi^2\left(z_p^2\right)^3}. \tag{8}$$

This means that the contours of $|B_p|^2$ allow us to compute the approximate position in 3-D of the ferrous contaminant by copying the x- and y-coordinates from the maximum of $|B_p|^2$ and estimating the z-coordinate from the distance away from the maximum at which the decay of the signal is a factor of 8. Once the coordinates (x_p, y_p, z_p) are estimated, the mass of the ferrous/steel part m_{steel} can be estimated by

$$m_{\text{steel}} = \alpha \rho_{\text{steel}} \frac{4\pi \left|\boldsymbol{B}_{p,\max}\right|}{B_x} z_p^3. \tag{9}$$

For the three 1-cm^3 steel objects, the factor $(4\pi|\boldsymbol{B}_{p,\max}|/B_x)z_p^3$ gives the values, as listed in Table II. From these data, the mass of steel can be estimated if the parameter α is properly selected. Based on the data in Table II and (9), the values of α which allow the mass estimation are 0.11, 0.29, and 0.10 for bolt, nut, and ring at $z_p = 2$ cm; and 0.10, 0.26, and 0.10 for bolt, nut, and ring at $z_p = 6$ cm, respectively. Therefore, a similar α can be used for a variable height of the object above the sensor plane, but α depends on the shape of the steel parts and may vary from 0.1 to 0.3. The best value for α to be used in practice depends on the statistics of the various types of steel attachments. It must therefore be calibrated experimentally by extracting a number of aluminum pieces with small steel contaminants and measuring their true mass, or by comparing them with results from the smelter.

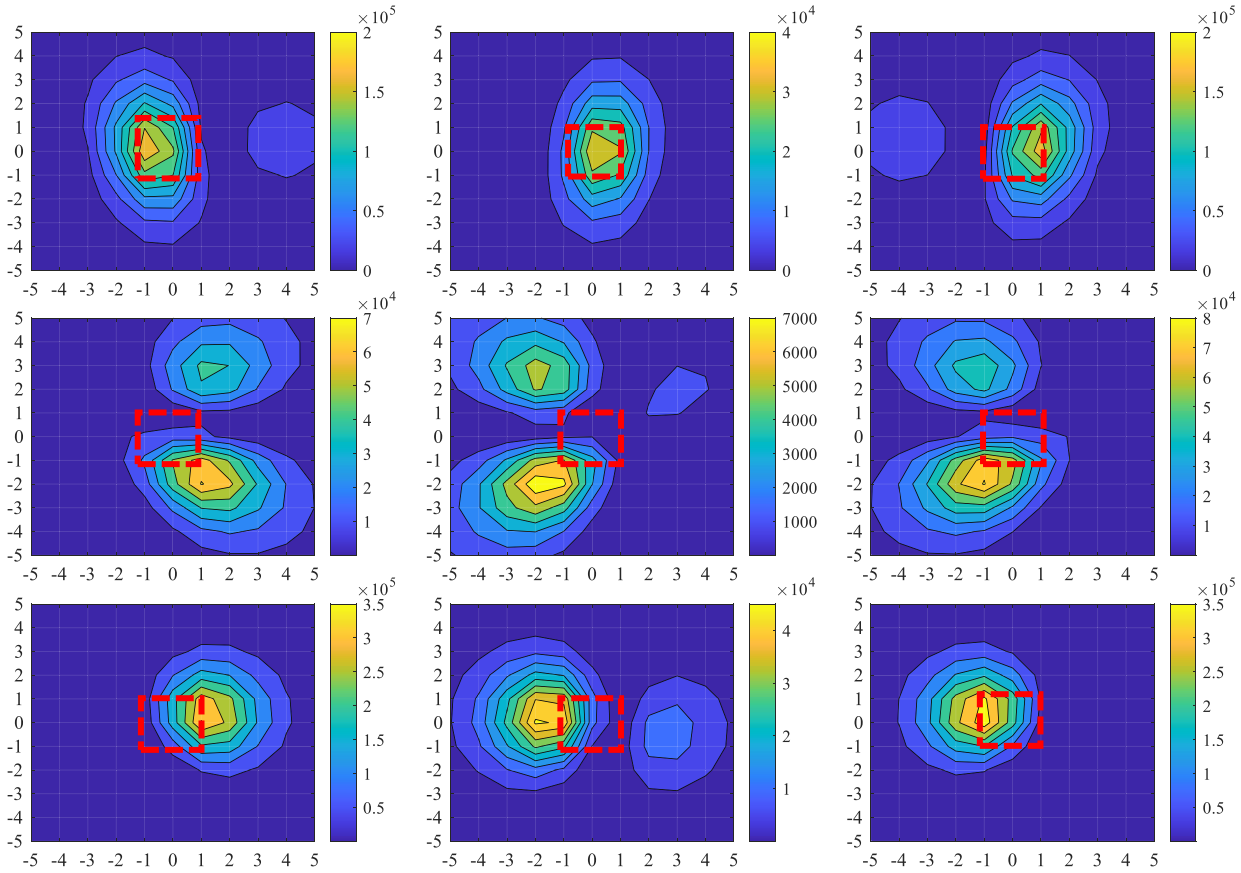

Fig. 6. Contours of $|B_{p,x}|^2$ (top), $|B_{p,y}|^2$(middle), and $|B_{p,z}|^2$ (bottom) for a bolt (left), a nut (middle), and a ring (right) in μT^2, 4 cm above the sensor plane. The red dashed boxes indicate the projected position within 1 cm from the ferrous piece.

TABLE I
VALUES OF THE DECAY FACTOR FOR $|\boldsymbol{B}_p|^2$ FROM $r = 0$ (MAXIMUM) TO $r = z_p$

$\sqrt{x^2+y^2} = z_p$ [cm]	Value for bolt	Value for nut	Value for ring
4	8.2	7.4	8.7

TABLE II
VALUES OF THE FACTOR $(4\pi|\boldsymbol{B}_{p,\mathrm{MAX}}|/B_x)z_p^3$

Height z_p [cm]	Values for bolt [cm^3]	Values for nut [cm^3]	Values for ring [cm^3]
2	9.3	3.5	9.7
6	10.0	3.8	10.3

B. Inversion for 1-D Sensors

Not all the measured components of the field contain equally interesting information. At the same time, it is interesting to reduce the data flow and the complexity of the sensor by measuring the field in one direction only, i.e., in the x-, y-, or z-direction. In Fig. 6, the contour plots of $|B_{p,x}|^2$, $|B_{p,y}|^2$, and $|B_{p,z}|^2$ are compared to see which is the most suitable component. The same three ferrous parts were used as in the previous analysis and the same orientation. All objects were located 4 cm above the sensor plane.

The data show that only the contours of $|B_{p,x}|^2$ present a simple picture for interpreting the ferrous contaminant. In fact, by varying the orientation of the parts, the other contour graphs split up in as many as four isolated peaks, whereas $|B_{p,x}|^2$ remained a single peak in all tests. Besides, like the peak of $|\boldsymbol{B}_p|^2$, the peak of $|B_{p,x}|^2$ is located within 1 cm from the projected position of the ferrous piece, as indicated by the red dashed squares. Therefore, compared with the contours of $|B_{p,y}|^2$ and $|B_{p,z}|^2$, the contours of $|B_{p,x}|^2$ allow a better estimation of the position of the ferrous object.

In contrast with the contours of $|\boldsymbol{B}_p|^2$, the peak of $|B_{p,x}|^2$ is not circular. The best option seems to estimate the height z_p of the piece above the sensor plane from the distance along the y-axis at which the decay of the signal is a factor of 7–8, as listed in Table III. Again, the amount of ferrous/steel part can be estimated from the maximum value $|B_{p,x,\max}|$

$$m_{\mathrm{steel}} = \alpha' \rho_{\mathrm{steel}} \frac{4\pi \left|B_{p,x,\max}\right|}{B_x} z_p^3. \tag{10}$$

For the three 1-cm^3 ferrous objects, the factor $(4\pi|B_{p,x,\max}|/B_x)z_p^3$ gives slightly more consistent values across the variation in shape than when using $|\boldsymbol{B}_{p,\max}|$ (Table IV). Based on the data in Table IV and (10), the values of α' which allow the mass estimation are 0.16, 0.33, and 0.18 for bolt, nut, and ring at $z_p = 2$ cm; and 0.14, 0.32, and 0.15 for bolt, nut, and ring at $z_p = 6$ cm, respectively.

TABLE III
VALUES OF THE DECAY FACTOR FOR $|B_{p,x}|^2$ FROM $r = 0$ (MAXIMUM) TO $r = z_p$

$\sqrt{x^2+y^2} = z_p$ [cm]	Value for bolt	Value for nut	Value for ring
4	6.7	7.8	8.3

TABLE IV
VALUES OF THE FACTOR $(4\pi|B_{p,x,\mathrm{MAX}}|/B_x)z_p^3$

Height z_p [cm]	Values for bolt [cm^3]	Values for nut [cm^3]	Values for ring [cm^3]
2	6.1	3.0	5.6
6	7.0	3.1	6.7

Considering the results that α' varies from 0.14 to 0.33, an initial (uncalibrated) estimate of α' may be $\alpha' = 0.24$.

C. Comparison of Pickup Coils and Hall Sensor for Bx

From the simulation data in Section III-B, it shows that an interesting option for the sensor array of a detection system for ferrous attachment is to use 1-D Hall elements or 1-D pickup coils, measuring the field or field changes parallel to the field lines of the magnet. Both types of arrays were made in the form of 32-cm-long sensor strips, one on either side of the belt guiding track in the middle of the conveyor of the experimental setup. In order to detect 1 cm^3 of a ferrous object moving at a speed of 2.5 m/s at 10 cm above the plane of the sensors, the Hall sensors need to have a sensitivity of about 10 μT and the pickup coils need to fit into a 1-cm^2 space in the yz plane and still be able to detect a field change of about 1 mT/s.

The 3-D Hall sensor array of the first experiment was replaced by two arrays for measuring B_x only. One array was a pickup coil array (each element 6-mm-diameter, 68-mH sensitivity), positioned at $x = 0$ (center of the magnet). The second was a 1-D Hall sensor array positioned at $x = 0.1$ m (0.1 m away from the center). The sampling rate of getting signal data from the ADC processed data of Hall sensors was increased to 400 Hz, corresponding to a pixel size of about 6 mm in the x-direction at a belt speed of 2.5 m/s.

The very small ferrous pieces (e.g., mass of about 2.2 g) were well detected at distances of 30 mm to the sensor arrays, which are the distances that occur most frequently for aluminum scraps in our industrial samples. At the same time, ferrous objects of larger sizes were clearly detectable with signals of 40–60 μT at 100 mm above the belt. Except for their z-axis being antiparallel, the results for the nut of 2.2 g at 22 mm height [Fig. 7(b)] were close to the results of the 3-D array [Fig. 4(a) and (d)]. The signal-to-noise ratio (SNR) was calculated as the ratio of the peak value of the signal to the root mean square (rms) of the data during the noise period, which covers the time from 0 to 0.4 s in Fig. 7(a) and (b). From the calculated SNR [Fig. 7(c) and (d)], the Hall sensors showed a slightly better SNR than the pickup coils.

D. Reduction of Signals From Aluminum Pieces

It is the aim of the sensor design not to detect aluminum (or nonferrous metal) pieces. Therefore, the field sensed by the array is estimated here for aluminum pieces, with the aim to optimize the position and sensitivity of the sensor and minimize signals produced by large aluminum scraps. The analysis is explained for a typical example scrap with a mass of 423 g, as shown in Fig. 8.

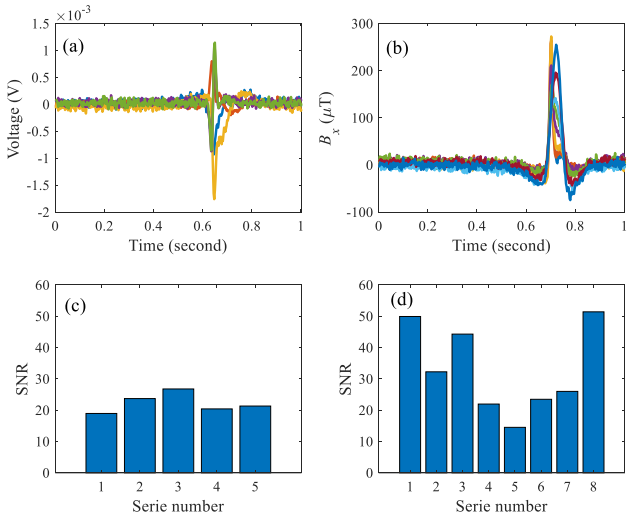

Fig. 7. Signals of a contaminant (No. 1, Nut, 2.2 g) measured from (a) 1-D pickup coils and (b) 1-D Hall sensors, where the data measured by different sensor series in the array are indicated by different line colors, and the SNR of different series from (c) 1-D pickup coils and (d) 1-D Hall sensors.

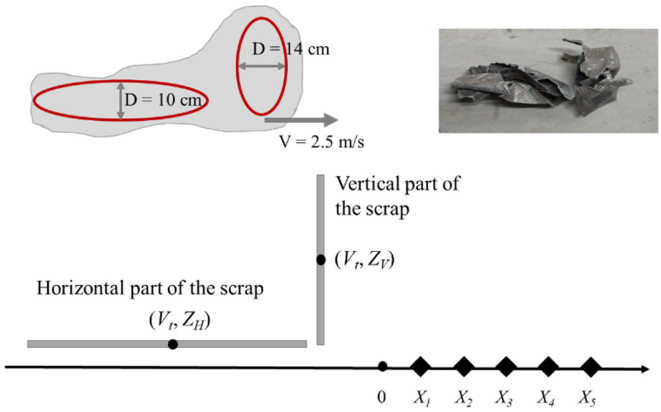

Fig. 8. Example of a very large piece of aluminum scrap with thickness $\delta = 2$ mm and a mass of 423 g (on average, 100–180-mm scrap particle mass is about 150 g). The piece has a high vertically oriented part of 14 cm diameter in both directions and an elongated horizontal part of 10 cm diameter and 24 cm length. The diagram and the photograph (top left and right) are as seen from the top of the conveyor belt. A model of the scrap and sensor array positions X_0–X_5 is shown at the bottom.

A piece of aluminum moving through a not entirely homogeneous field produces eddy currents, which in turn may produce a detectable field. The simplest case for theoretical analysis is a flat disk of aluminum with diameter D, sheet thickness δ, and electrical conductivity σ, which is subjected to a harmonically fluctuating field with an amplitude $\boldsymbol{A}$ (tesla) and a circular frequency ω (rad/s) oriented perpendicularly to the disk, i.e.,

$$\boldsymbol{B} = \mathrm{Re}\{\boldsymbol{A}e^{i\omega t}\} = \boldsymbol{A}\cos(\omega t). \tag{11}$$

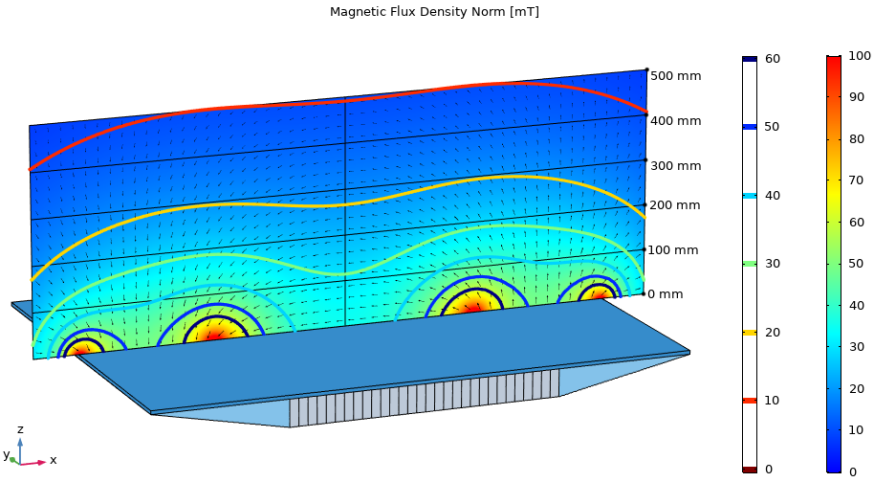

Fig. 9. Field strength distribution of the magnet used in the experiments. The colored lines show contours of $|\boldsymbol{B}|$ (mT).

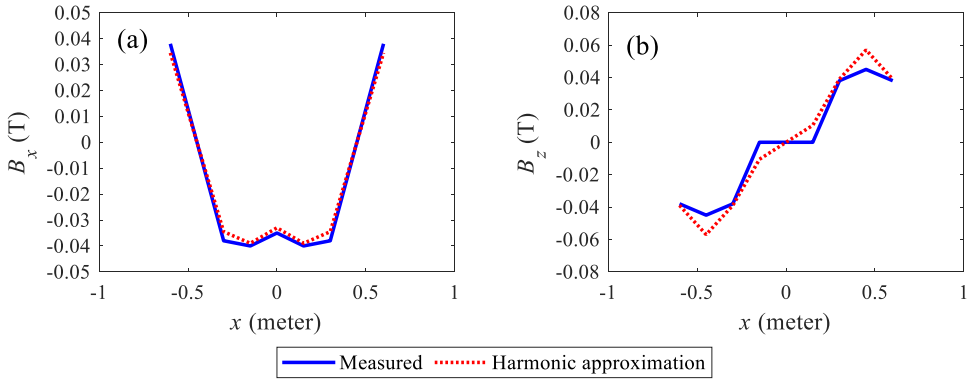

Fig. 10. Measured and harmonic approximation of field components (a) B_x and (b) B_z as a function of x at $z = 0.07$ m.

In general, the magnetic moment of such a disk as a result from eddy currents can be approximated by [30]

$$\begin{aligned}\boldsymbol{m} &= -\frac{D^3}{6\mu_0}\mathrm{Re}\left\{\frac{i\,\mu_0\omega\sigma\,D\delta}{\frac{64}{3\pi}+0.8\,i\,\mu_0\omega\sigma\,D\delta}\boldsymbol{A}e^{i\omega t}\right\}\\ &= -\boldsymbol{A}\frac{D^3}{6\mu_0}\left\{\frac{0.8\omega^2\tau^2\cos\omega t - C\omega\tau\sin\omega t}{C^2+0.64\omega^2\tau^2}\right\}\\ \tau &= \mu_0\sigma\,D\delta;\quad C=\frac{64}{3\pi}.\end{aligned} \tag{12}$$

For the conditions and parameters of the scrap pieces and the sensor system, the $\cos\omega t$ term can be neglected since the ratio $0.8\omega\tau/C$ is less than 5% for typical angular frequencies experienced by the scrap. Therefore, the self-induction or mutual induction of eddy currents is neglected and the expression for the magnetic moment is simplified to

$$\boldsymbol{m} = \boldsymbol{A}\frac{\pi D^3}{128\mu_0 C}\mu_0\omega\sigma\,D\delta\tau\sin\omega t. \tag{13}$$

In this limit, the eddy current distribution in the disk ($0 \le r \le D/2$) is given by [30]

$$J(r)\left[\frac{\mathrm{A}}{\mathrm{m}}\right] = \frac{A\omega\sigma\,\delta r}{2}\sin\omega t. \tag{14}$$

In order to evaluate the fluctuations of the field that are experienced by the piece of scrap and estimate values for A and ω, the field distribution of the magnet (Fig. 9) that was used in the experiments was sampled at a height of 0.07 m above the magnet and fit with harmonics, as shown in Fig. 10.

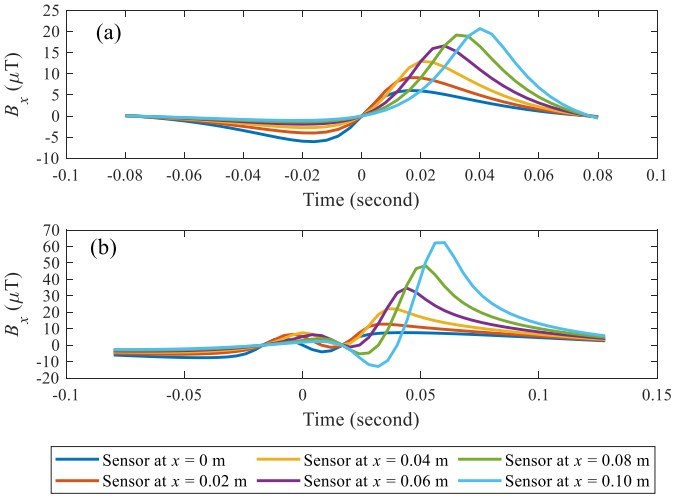

Fig. 11. Simulated signals produced by eddy currents in (a) vertical part and (b) horizontal part of a large piece of aluminum scrap at a range of sensor positions (x from 0 to 0.10 m).

The approximation of the field that fits the data and Maxwell's equations can be based on Fourier series

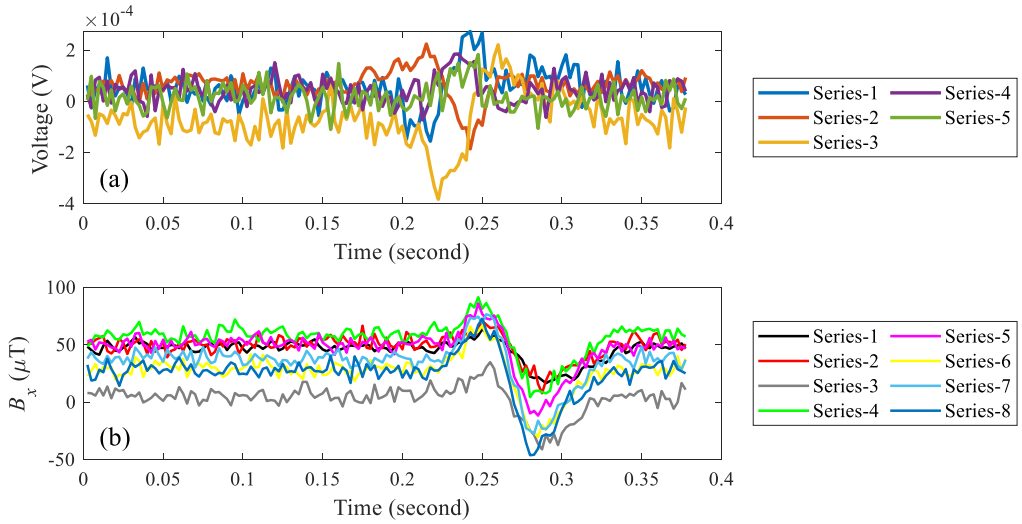

Fig. 12. Measured signals sampled at 400 Hz for the aluminum piece of Fig. 8. (a) Pickup coil array at $x = 0$ m. (b) Hall array at $x = 0.1$ m.

representation [18], given by

$$B_x = A_1 e^{-\pi z/P} \cos(\pi x/P) + A_3 e^{-3\pi z/P} \cos(3\pi x/P) \quad (15)$$

$$B_z = -A_1 e^{-\pi z/P} \sin(\pi x/P) - A_3 e^{-3\pi z/P} \sin(3\pi x/P). \quad (16)$$

Therefore, for a scrap particle moving with velocity V (i.e., $x = Vt$) at constant height z above the magnet, the field seems to fluctuate with two harmonic components, $\omega_1 = \pi V/P$ and $\omega_3 = 3\pi V/P$

$$B_x = A_1 e^{-\pi z/P} \cos(\pi Vt/P) + A_3 e^{-3\pi z/P} \cos(3\pi Vt/P) \quad (17)$$

$$B_z = -A_1 e^{-\pi z/P} \sin(\pi Vt/P) - A_3 e^{-3\pi z/P} \sin(3\pi Vt/P). \quad (18)$$

Since aluminum scrap particles are widely shaped and an exact simulation is anyway not intended, the aim here is to get an indication of the field detected by the sensor and understand the options for optimization of the sensor position. Accordingly, the maximum field that is picked up by the sensors from the circulating currents at the boundary of the scrap is estimated by approximating the eddy current distributions in the horizontal (H) and vertical (V) parts of the scrap particle instance by simple unidirectional currents

$$\text{H-part:} J_y(x', z_H) = \frac{\sigma\delta(x' - Vt)}{2}\{A_1\omega_1 e^{-\pi z_H/P}\cos(\pi Vt/P) + A_3\omega_3 e^{-3\pi z_H/P}\cos(3\pi Vt/P)\} \quad (19)$$

$$\text{V-part:} J_y(Vt, z') = -\frac{\sigma\delta(z - z_V)}{2}\{A_1\omega_1 e^{-\pi z_V/P}\sin(\pi Vt/P) + A_3\omega_3 e^{-3\pi z_V/P}\sin(3\pi Vt/P)\}. \quad (20)$$

This then leads to the following estimates for the maximum field signal at the sensor positions if the sensor array is positioned at alternative locations ($x = x_i, z = 0$) along the length of the magnet

$$\text{H-part:} B_{p,x} = -\int_{\xi=-D/2}^{D/2} \frac{\mu_0 J_y(Vt + \xi, z_H)\mathrm{d}\xi}{2\pi\sqrt{(Vt + \xi - x_i)^2 + z_H^2}} \quad (21)$$

$$\text{V-part:} B_{p,x} = -\int_{\zeta=-D/2}^{D/2} \frac{\mu_0 J_y(Vt, z_V + \zeta)\mathrm{d}\zeta}{2\pi\sqrt{(Vt - x_i)^2 + (z_V + \zeta)^2}}. \quad (22)$$

The parameters of the approximation of the field A_1, A_3, P, and V are -0.055 T, 0.028 T, 0.9 m, and 2.5 m/s, respectively. The resulting simulated field from eddy currents at sensor positions in the middle of the magnet and at distances of 20, 40, 60, 80, and 100 mm from the middle is shown in Fig. 11. The signals for the real piece of scrap shown in Fig. 8 were also measured by the two sensor arrays at $x = 0$ m and at $x = 0.1$ m, and these signals are shown in Fig. 12. The results indicate that the Hall array signals are likely to have been produced by the horizontal part of the scrap since the measured and simulated signals for position $x = 0.1$ m have a similar magnitude and roughly identical shapes, particularly for the Hall array series 1, 2, 4, and 5.

The Hall array signal from the very large aluminum piece is about 60 μT. It was checked that there were no ferrous parts hidden in the aluminum and the signal is not from vibration or tilting of the sensor array caused by the passing scrap particle. Since the noise level of the sensor is about 10 μT and the signal from small steel contaminants at 100 mm from the belt surface is about 40–60 μT, it is interesting to reduce the eddy current signals from the aluminum scrap by a factor of 3–4 to below 20 μT. One option is to optimize the position of the sensor array, as shown by the results in Fig. 11. The differences between the signals at $x = 0$ m and at $x = 0.1$ m suggest that a significant reduction can be achieved by such position optimization. Another route

is to take away the inhomogeneities of the field shown in Figs. 9 and 10.

IV. Conclusion

In this work, we presented a magnetic image sensor that can identify small ferrous contaminants (including their estimated mass and positions) in large nonferrous scraps (e.g., aluminum scraps with screen passing size 100–180 mm) in a sorting processing line. Specifically, the sensor can detect small ferrous pieces (e.g., nuts, screws, and bolts) in the mass range of 2–16 g within 100 mm from the surface of the conveyor belt.

The sensor signal can be interpreted into the 3-D location of the ferrous piece within 10 mm from its actual position, by a proposed inversion algorithm. The mass of the ferrous contaminant can typically be estimated up to a factor of 2 or 3, which can be improved through calibration with contaminants found in actual scrap flows.

For the design of the sensor, both computational and experimental results showed that it is feasible to use 1-D Hall elements or 1-D pickup coils for the sensor array to measure the field or field changes parallel to the field lines of the magnet, while the Hall elements showed a slightly better SNR than the pickup coils.

Because the magnetic field of the used magnet was not entirely homogeneous, the passing of very large aluminum pieces (or some other nonferrous pieces) may lead to relatively large eddy currents and corresponding disturbing signals. To reduce such disturbing signals, two options are proposed: the first is to optimize the position of the array along the direction of motion near the center of the sensor volume; and the second is to further reduce the field inhomogeneities of the magnet, which are the cause of the signals from the aluminum/nonferrous scrap particles.

Overall, the presented magnetic image sensor is promising to recognize nonferrous scraps with small ferrous contaminants and achieve high-precision sorting tasks. It is noted that the sensor and obtained findings in this study are not limited to the applications regarding aluminum or nonferrous scraps but can be more widely used in many other scenarios where the mass ratio of the ferrous contaminant to the main material is small. Moreover, this sensor can also be installed together with an AI recognition system in a sorting line, and thus, it can help to: 1) realize more accurate sorting results based on sensor fusion and/or 2) continuously validate and train AI systems for recognizing bolts, nuts, and rings, from nonferrous and/or stainless metals. Such work is ongoing in collaboration with Dutch company Myne in the development of a digital-on-demand recycling plant, and more results will be reported in future.

Appendix I
Derivation of (6)

With $\vartheta = (\pi/2)$, $\varphi = 0$, (4) can be simplified as

$$\boldsymbol{m} = \frac{V_p B_x}{\mu_0}\begin{pmatrix}\frac{1}{D_b}\\0\\0\end{pmatrix} = \begin{pmatrix}\frac{V_p B_x}{D_b \mu_0}\\0\\0\end{pmatrix}.$$

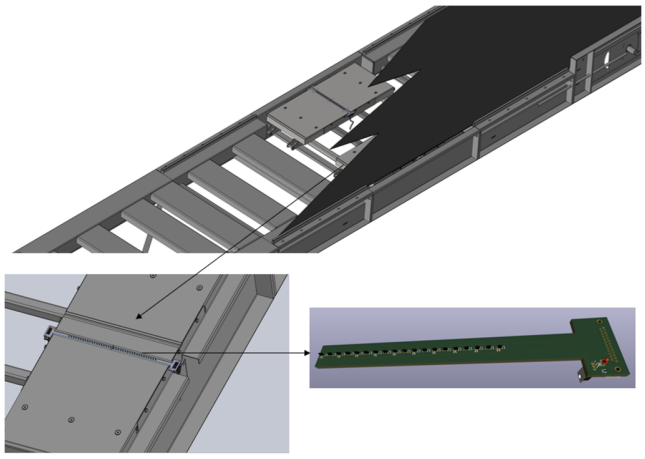

Fig. 13. Layout of the magnetic image sensor implemented in a processing line, where the top plot shows the overall view of the two sensor arrays at the left and right sides of the guiding track under the belt (each array is placed at the middle of the magnet inside the box underneath the array), and the bottom-left plot shows the enlarged view of an array that includes two sensor strips (bottom-right plot) with a series of magnetic field sensors (black elements).

Then, (6) can be derived from (5) as follows:

$$\begin{aligned}
&\left(B_{px}, B_{py}, B_{pz}\right)\\
&= \frac{\mu_0}{4\pi r^5}\left(3(\boldsymbol{m}\cdot\boldsymbol{r})\boldsymbol{r} - \boldsymbol{m}\cdot r^2\right)\\
&= \frac{\mu_0}{4\pi r^5}\left(3\left(-\frac{V_p B_x}{D_b \mu_0} v\left(t-t_p\right)\right)\begin{pmatrix}-v\left(t-t_p\right)\\-\Delta y_i\\-\Delta z\end{pmatrix}\right.\\
&\qquad\left. - \begin{pmatrix}\frac{V_p B_x}{D_b \mu_0}\\0\\0\end{pmatrix}\cdot r^2\right)\\
&= \frac{\mu_0}{4\pi r^5}\left(3\frac{V_p B_x}{D_b \mu_0}\begin{pmatrix}v^2\left(t-t_p\right)^2\\v\left(t-t_p\right)\Delta y_i\\v\left(t-t_p\right)\Delta z\end{pmatrix}\right.\\
&\qquad\left. - \begin{pmatrix}\frac{V_p B_x}{D_b \mu_0}\\0\\0\end{pmatrix}\cdot\left(v^2\left(t-t_p\right)^2 + \Delta y_i^2 + \Delta z^2\right)\right)\\
&= \frac{\mu_0}{4\pi r^5}\left(\frac{V_p B_x}{D_b \mu_0}\begin{pmatrix}2v^2\left(t-t_p\right)^2 - \Delta y_i^2 - \Delta z^2\\3v\left(t-t_p\right)\Delta y_i\\3v\left(t-t_p\right)\Delta z\end{pmatrix}\right)\\
&= \frac{V_p B_x}{4\pi D_b\left(v^2\left(t-t_p\right)^2 + \Delta y_i^2 + \Delta z^2\right)^{2.5}}\\
&\quad\times\begin{pmatrix}2v^2\left(t-t_p\right)^2 - \Delta y_i^2 - \Delta z^2\\3v\left(t-t_p\right)\Delta y_i\\3v\left(t-t_p\right)\Delta z\end{pmatrix}.
\end{aligned}$$

Besides, if ϑ and φ are changed to another set, e.g., $\vartheta = 0$ and $\varphi = (\pi/2)$, then (4) and (6) can also be easily changed as

$$\boldsymbol{m} = \frac{V_p B_x}{\mu_0}\begin{pmatrix}\frac{1}{D_a}\\0\\0\end{pmatrix} = \begin{pmatrix}\frac{V_p B_x}{D_a \mu_0}\\0\\0\end{pmatrix}$$

$$\left(B_{px}, B_{py}, B_{pz}\right) = \frac{V_p B_x}{4\pi D_a \left(v^2\left(t-t_p\right)^2 + \Delta y_i^2 + \Delta z^2\right)^{2.5}} \times \begin{pmatrix} 2v^2\left(t-t_p\right)^2 - \Delta y_i^2 - \Delta z^2 \\ 3v\left(t-t_p\right)\Delta y_{i.} \\ 3v\left(t-t_p\right)\Delta z \end{pmatrix}.$$

Appendix II
Sensor Layout in Implementation

See Fig. 13

Acknowledgment

The authors would like to thank the anonymous reviewers whose comments and suggestions helped them improve the quality of the article.

References

[1] E. Aluminium, *Vision 2050: European Aluminium's Contribution to the EU's Mid-Century Low-Carbon Roadmap*. Brussels, Belgium, 2019.

[2] F. Di Maio and P. C. Rem, "A robust indicator for promoting circular economy through recycling," *J. Environ. Protection*, vol. 6, no. 10, pp. 1095–1104, 2015.

[3] M. A. Reuter, "Digitalizing the circular economy," *Metall. Mater. Trans. B*, vol. 47, no. 6, pp. 3194–3220, Dec. 2016.

[4] E. Van Der Voet, L. Van Oers, M. Verboon, and K. Kuipers, "Environmental implications of future demand scenarios for metals: Methodology and application to the case of seven major metals," *J. Ind. Ecol.*, vol. 23, no. 1, pp. 141–155, Feb. 2019.

[5] D. Raabe et al., "Making sustainable aluminum by recycling scrap: The science of 'dirty' alloys," *Prog. Mater. Sci.*, vol. 128, Jul. 2022, Art. no. 100947.

[6] J. Oberteuffer, "Magnetic separation: A review of principles, devices, and applications," *IEEE Trans. Magn.*, vol. MAG-10, no. 2, pp. 223–238, Jun. 1974.

[7] G. Gaustad, E. Olivetti, and R. Kirchain, "Improving aluminum recycling: A survey of sorting and impurity removal technologies," *Resour., Conservation Recycling*, vol. 58, pp. 79–87, Jan. 2012.

[8] D. Díaz-Romero, W. Sterkens, S. Van den Eynde, T. Goedemé, W. Dewulf, and J. Peeters, "Deep learning computer vision for the separation of cast- and wrought-aluminum scrap," *Resour., Conservation Recycling*, vol. 172, Sep. 2021, Art. no. 105685.

[9] S. Koyanaka and K. Kobayashi, "Automatic sorting of lightweight metal scrap by sensing apparent density and three-dimensional shape," *Resour., Conservation Recycling*, vol. 54, no. 9, pp. 571–578, Jul. 2010.

[10] D. W. Hahn and N. Omenetto, "Laser-induced breakdown spectroscopy (LIBS)—Part II: Review of instrumental and methodological approaches to material analysis and applications to different fields," *Appl. Spectrosc.*, vol. 66, no. 4, pp. 347–419, Apr. 2012.

[11] Y. Dai, S. Zhao, C. Song, and X. Gao, "Identification of aluminum alloy by laser-induced breakdown spectroscopy combined with machine algorithm," *Microw. Opt. Technol. Lett.*, vol. 63, no. 6, pp. 1629–1634, Jun. 2021.

[12] M. B. Mesina, T. P. R. de Jong, and W. L. Dalmijn, "Automatic sorting of scrap metals with a combined electromagnetic and dual energy X-ray transmission sensor," *Int. J. Mineral Process.*, vol. 82, no. 4, pp. 222–232, Jun. 2007.

[13] M. B. Mesina, T. P. R. de Jong, and W. L. Dalmijn, "Improvements in separation of non-ferrous scrap metals using an electromagnetic sensor," *Phys. Separat. Sci. Eng.*, vol. 12, no. 2, 2003, Art. no. 180856.

[14] M. D. O'Toole, N. Karimian, and A. J. Peyton, "Classification of nonferrous metals using magnetic induction spectroscopy," *IEEE Trans. Ind. Informat.*, vol. 14, no. 8, pp. 3477–3485, Aug. 2018.

[15] A. Sheinker, B. Ginzburg, N. Salomonski, P. A. Dickstein, L. Frumkis, and B.-Z. Kaplan, "Magnetic anomaly detection using high-order crossing method," *IEEE Trans. Geosci. Remote Sens.*, vol. 50, no. 4, pp. 1095–1103, Apr. 2012.

[16] T. Ram-Cohen, R. Alimi, E. Weiss, and Z. Zalevsky, "Characterization and detection of oscillating magnetic dipole signals," *Meas. Sci. Technol.*, vol. 28, no. 4, Apr. 2017, Art. no. 045104.

[17] H. Liu, X. Zhang, H. Dong, Z. Liu, and X. Hu, "Theories, applications, and expectations for magnetic anomaly detection technology: A review," *IEEE Sensors J.*, vol. 23, no. 16, pp. 17868–17882, Aug. 2023.

[18] E. Weiss and R. Alimi, *Low-Power and High-Sensitivity Magnetic Sensors and Systems*. Norwood, MA, USA: Artech House, 2018.

[19] M. N. Nabighian et al., "The historical development of the magnetic method in exploration," *Geophysics*, vol. 70, no. 6, p. 3, Nov. 2005.

[20] W. F. Hanna, "Some historical notes on early magnetic surveying in the U.S. geological survey," in *Geologic Application of Modern Aeromagnetic Surveys*. Washington, DC, USA: U.S. Geological Survey Bulletin, U.S. Government Printing Office, 1990, pp. 63–73.

[21] S. Song, X. Qiu, J. Wang, and M. Q.-H. Meng, "Design and optimization strategy of sensor array layout for magnetic localization system," *IEEE Sensors J.*, vol. 17, no. 6, pp. 1849–1857, Mar. 2017.

[22] P. Ripka and M. Janosek, "Advances in magnetic field sensors," *IEEE Sensors J.*, vol. 10, no. 6, pp. 1108–1116, Jun. 2010.

[23] M. A. Khan, J. Sun, B. Li, A. Przybysz, and J. Kosel, "Magnetic sensors—A review and recent technologies," *Eng. Res. Exp.*, vol. 3, no. 2, Jun. 2021, Art. no. 022005.

[24] P. C. Rem, S. P. M. Berkhout, and C. Van Beek, *Apparatus and Method for Picking Up Objects Off a Surface*, document WO2020242298A1, 2020.

[25] P. C. Rem, Y. Wu, and F. Di Maio, *Recycling of Scrap*, document WO2023224478A1, 2023.

[26] P. C. Rem, Y. Wu, and F. Di Maio, *Recycling of Scrap (Scrap Selector Infeed)*, document NL2031877B1, 2023.

[27] P. C. Rem, Y. Wu, and F. Di Maio, *Recycling of Scrap (Scrap Selector Ejector)*, document NL2031878B1, 2023.

[28] P. C. Rem, Y. Wu, and F. Di Maio, *Recycling of Scrap (Scrap Selector Process Layout)*, document NL2031879B1, 2023.

[29] W. Wynn, C. Frahm, P. Carroll, R. Clark, J. Wellhoner, and M. Wynn, "Advanced superconducting gradiometer/magnetometer arrays and a novel signal processing technique," *IEEE Trans. Magn.*, vol. MAG-11, no. 2, pp. 701–707, Mar. 1975.

[30] P. C. Rem, *Eddy Current Separation*. Delft, The Netherlands: Eburon, 1999, pp. 123–125.

Yongli Wu received the B.Eng. and M.Eng. degrees in metallurgical engineering from Northeastern University, Shenyang, China, in 2013 and 2015, respectively, and the Ph.D. degree in chemical engineering from Monash University, Clayton, VIC, Australia, in 2019.

From 2019 to 2023, he conducted postdoctoral research at the SEU-Monash Joint Research Institute, Suzhou, China, and Delft University of Technology, Delft, The Netherlands. Since 2023, he has been an Assistant Professor with the Section of Resources and Recycling, Delft University of Technology. His research interests include digital recycling, sensor-based sorting, particle technology, computational modeling, and the circularity of materials.

Dr. Wu was awarded a Marie Skłodowska-Curie Postdoctoral Fellowship in 2022.

Tijmen Oudshoorn was born in The Hague, The Netherlands, in 1991. He received the bachelor's and master's degrees in industrial design engineering from Delft University of Technology, Delft, The Netherlands, in 2017.

Since 2017, he has been with Myne Circular Metals, Harderwijk, The Netherlands, as a Project Engineer in Aluminium Recycling. In this role, he focuses on designing, detailing, and producing prototypes used both in the University Laboratory and in pilot plants in Harderwijk. He is particularly involved in the development of vision systems that identify and classify various types of scrap metal, as well as the integrated design, development, and testing of experimental setups for automated scrap metal recycling systems. He holds one patent, WO2022189165A1, which originated from his graduate thesis project and describes an installation for separating seashells from beach debris. He is also the co-author of journals and conference papers in metal recycling fields. In his current position, he works with RGB, 3-D, XRT, and LIBS sensors to classify scraps. His research interests include nonferrous metal recycling by vision systems and magnetic density separation. He is dedicated to advancing sustainable practices in metal recycling through innovative design and technology.

Rik Mulder received the B.Sc. degree in technology and liberal arts and sciences from the University of Twente, Enschede, The Netherlands, in 2018, and the M.Sc. degree in artificial intelligence from The University of Edinburgh, Edinburgh, U.K., in 2019.

From 2019 to 2023, he worked as a Freelance AI Engineer, including significant roles at BandenConcurrent B.V., Eindhoven, The Netherlands, and Myne Circular Metals, Harderwijk, The Netherlands. Since 2024, he has been the Chief Technology Officer of BandenConcurrent B.V.

Kees van Beek was born in Sassenheim, South Holland, The Netherlands, in 1956. He studied Electrical Engineering from Delft University of Technology (TU Delft), Delft, The Netherlands. He received the bachelor's degree in electronic engineering from Amsterdam HTS.

He has been at the Process Engineering Department, Siemens, since 1986. He has been the Head of the Measurement and Control Support Group, TU Delft, since 2000. He developed several new hardware and software solutions for measurement and control of complex research setups (e.g., sensors and complete systems). Since 2023, he has been retired, but still working part time at TU Delft.

Peter Rem received the Ph.D. degree in physics from Twente University, Enschede, The Netherlands, in 1986.

He is currently an Emeritus Professor, having chaired the Resources and Recycling Section, Delft University of Technology, Delft, until 2024. The Resources and Recycling Section received national and international prizes for its work on recycling of concrete, the recycling of polymers, and the extraction of phosphate from sewage sludge, and built patent portfolios for spinouts operating worldwide.